Finite difference stencils based on particle strength exchange schemes for improvement of vortex methods

Philippe Poncet

Revised version for Journal of Turbulence, JOT/188260/SPE

Finite difference stencils based on particle strength exchange schemes for improvement of vortex methods

Philippe Poncet

Dept. GMM, INSA, 135 avenue de Rangueil, 31077 Toulouse Cedex 4, France

Abstract

The method of Particle Strength Exchange, solving the viscous part of the Navier-Stokes equations by a splitting time algorithm in the context Vortex Methods. This article presents a few results on the numerical aspects of this Lagrangian diffusion scheme, that is to say computation of the Laplacian of a measure function. The present work follows the classical analysis by Degond and MasGallic whose formulas were obtained by means of integration of continuous functions. One shows that one gets different operators when integration is discrete, and leads to a substantial gain of accuracy. This scheme is then applied to several three-dimensional flows to exhibit convergence rate, and impact on conservation laws at moderate Reynolds numbers. A sensitivity analysis is finally provided in order to carry out the good behavior of these schemes in both Eulerian and Lagrangian contexts.

1 Introduction

Estimation of particle diffusion is of fundamental interest for particle methods which aim at solving numerically equations containing a parabolic part, such as the heat transport, the Navier-Stokes equations, Fokker-Planck equations and many others. In this paper, a new approach of Particle Strength Exchange methods is proposed in order to provide a gain of accuracy compared to classical formulations, which holds for both Eulerian and Lagrangian contexts, that is to say for grids as well as for sets of particles non uniformly dispatched.

Indeed, classical formulation of particle strength exchange, originally developed by Degond and MasGallic [7], involves particles arbitrarily dispatched. This particle diffusion method performed by means of a kernel technique has been successfully used in many high-resolution complex flow computations (see [12, 13, 3, 15, 5] for instance).

The convergence of the method is obtained in the sense that the error is of order of $(h/\varepsilon)^2$ where h is the characteristic distance between particles and ε the width of the diffusion kernel. The convergence consequently holds as $h/\varepsilon \to 0$. The main drawback of such a scheme is that as resolution increases, *i*.e. as h decreases, one usually does not want to have the number of connections between the knots involved in the scheme increasing, in order to focus on smaller scales and to have a computational cost depending reasonably on the number of grid points or particles. This comes to assume that the refinement process is performed with h/ε more or less constant. Once again a major drawback is that PSE schemes are not intrinsically consistent in h but only in h/ε, thus a lack of accuracy when grids or particle lattices are refined.

The present paper presents a technique of renormalization so that particle strength exchange schemes are intrinsically consistent as h^2 when grids are uniformly discretized. This approach is in a first step totally equivalent to a finite difference scheme. In some cases of singular functions the

renormalized PSE scheme, called discrete PSE scheme, exhibits a better behavior but in general one reaches the same accuracy and the same convergence rate as with standard finite differences.

The main advantage of this discrete PSE scheme is that it also holds in a Lagrangian context, that is to say when particles are dispatched in a non uniform grid. One obtains a self normalized scheme which is numerically better than classical PSE when Lagrangian distribution of particles is statistically uniformly dispatched. This is the case when used in conjunction with Vortex in Cell methods for which frequent remeshing is performed. One then obtains an interesting scheme in terms of accuracy that can be assimilated to a self adaptating finite difference scheme, based on a spherically symmetric stencil generator function.

Such considerations are especially interesting when performing direct numerical simulations of flows with a particle method (Smoothed Particle Hydrodynamics or Vortex in Cell methods) at low and moderate Reynolds numbers. Indeed, in this case, viscous effects need to be computed accurately since they are potentially of the same order as convective effects. Such accurate three-dimensional DNS simulations has been successfully performed in the past (see [15, 12, 6]).

The paper outline is as follows. Section 2 presents basically the spirit of Hybrid Vortex in Cell methods (2.1 and 2.2) and how diffusion is involved in the related algorithm in section 2.3. The classical formulation of particle strength exchange is then presented in section 2.4 for the computation of the diffusion process in the spherically symmetric and three-dimensional case. In section 3, the renormalization technique is presented, and is proved to be second order convergent on a Gaussian blob (in section 3.3).

A case presenting less regularity, the ring vortex, is developed in section 4. Indeed, the Laplacian of the field of vorticity of the ring presents a rational singularity on the symmetry axis, stronger as the ring core radius is smaller. Finite differences and discrete PSE are compared on this static example. The ring is chosen as initial condition to run a full three-dimensional Navier-Stokes simulation using the Vortex in Cell method presented previously. The impact on the kinetic energy conservation law of the numerical scheme (discrete PSE or finite differences) chosen to compute diffusion is then discussed.

In order to push further the lack of regularity of initial condition and study further the impact of diffusion schemes on the conservation laws, the case of a Gaussian blob of random vorticity field is presented in section 5. Random fields are indeed the worst imaginable case to study the impact of lack of regularity of solutions.

The benchmarks presented above are defined in Cartesian coordinates, within periodic boxes or with far field no-slip-through conditions, that is to say without boundary layers in both the formalisms of boundary conditions. In order to check that the method presented herein is a valid approach for more complex flows involving boundary layers and different from Cartesian coordinates, one considers in section 6 the interaction between a vortical ring (self propagating) and a solid cylindrical boundary on which the boundary layer interacts with the main ring of vorticity.

The discrete PSE being proved convergent and sufficiently accurate to run complex flow simulation in a general context, one discusses in section 7 the behavior of this scheme in a Lagrangian context, *i*.e. when particles are not uniformly dispatched on a grid. To proceed, point locations on a uniformly discretized grid are noised with a Gaussian random variable. Influence of the noise amplitude, that is to say the standard deviation of the Gaussian law considered, is discussed on the case of the scalar blob introduced in section 3.3. One considers several stencil width to show that accuracy can be tuned easily with the discrete formulation of particle strength exchange, which takes all its interest in this case.

2 Fluid mechanics context and classical results

2.1 Hybrid Vortex in Cell methods

One considers the three-dimensional Navier-Stokes equations in their velocity-vorticity formulation (u, ω) in a domain Ω whose boundary $\partial\Omega$, if it exists, is a body on which one has a no-slip condition. One considers also that the flow is without stream, that is to say the far-field velocity is zero. These equations reads :

$$\begin{cases} \dfrac{\partial \omega}{\partial t} + u \cdot \nabla \omega - \omega \cdot \nabla u - \nu \Delta u = 0 \ \ in \ \ \Omega \times]0, T[\\ \lim\limits_{|x| \to \infty} u(x,t) = 0 \ \ for \ all \ t \in]0, T[\\ u(x,t) = 0 \ \ on \ \ \partial\Omega \times]0, T[\\ \omega(x,0) = \omega_0(x) \ \ on \ \ \Omega \end{cases} \tag{1}$$

where the velocity field u is linked to the vorticity field ω by the relations

$$\mathrm{curl} u = \omega \ and \ \ \mathrm{div} u = 0 \ on \ \Omega, \ \ u \cdot \vec{n} = 0 \ on \ \partial\Omega \tag{2}$$

where $\vec{n}$ is the outward normal field to $\partial\Omega$ in the no-slip-through relation, which is included in the no-slip condition $u = 0$ in equation (1).

Vortex-in-Cell methods consist in introducing a set of particle (or cells) which are triplets of location-vorticity-volume $(x_p, \omega_p, v_p)_{p=1..n}$, which gives a Dirac expression for the vorticity field :

$$\omega = \sum_{p=1}^{n} \omega_p \delta_{x_p} v_p \tag{3}$$

In the present paper, the Vortex in Cell scheme is based on those detailled in [2] and [5]. Beneath are developed essential points to understand how parabolic equations are involved in these schemes.

At any time, the field u can be reconstructed from ω by a linear operator $\mathcal{A}\omega = u$ which is based on the resolution of a vectorial Poisson equation. A usual approach for vortex methods is to write $\mathcal{A}$ using the Biot-Savart laws

$$u(x) = \mathcal{A}\omega(x) = \omega * K_\varepsilon \int_\Omega K_\varepsilon(y - x)\omega(y) \, \mathrm{d}y = \sum_{p=1}^{n} K_\varepsilon(x_p - x)\omega_p v_p \, \mathrm{d}y$$

where K_ε is a mollified Green kernel. In practice, the evaluation of these formulas is computationally improved by multipole or tree-code methods, but it appears that for large amount of particles which are distributed volumically (that is to say not distributed on a sheet of vortex), hybrid methods are faster and sufficiently accurate.

Hybrid method consists in interpolating the pointwise field ω on a grid (or on $\mathbb{R}^3$) by means of a kernel Λ of class $\mathcal{C}^k$ (cf. [11]). This transfer reads as the convolution

$$\overline{\omega} = \omega * \Lambda : (\mathbb{R}^3 \times \mathbb{R}^3 \times \mathbb{R})^n \equiv \mathbb{R}^{7n} \to \mathcal{C}^k(\mathbb{R}^3)^3 \tag{4}$$

Then the stream Ψ is introduced, solution of a vectorial Poisson equation solved component by component $-\Delta\Psi = \overline{\omega}$ (equations are uncoupled in Cartesian coordinates).

One has to choose appropriate boundary conditions depending on the context : periodic cube or a combination of homogeneous Neumann and Dirichlet conditions that imply both $\mathrm{div}\Psi = 0$

and $\mathrm{curl}u \cdot \vec{n} = 0$ on boundaries (cf. [2]). This equation is solved either by a fast second or fourth order finite differences solver or by fast Fourier transforms in the periodic case. In more general systems of coordinates, a fourth component, called potential stream, is introduced in order to obtain four uncoupled elliptic equations instead of three coupled (for more details see [5]). One can notice that since ω is supposed divergence free, $\mathrm{div}\Psi = 0$ everywhere and $\overline{u} = \mathrm{curl}\Psi$ (in the case of Cartesian coordinates) satisfies all the conditions (2).

Numerically, the velocity field $\overline{u}$ is obtained on a grid of size N (containing N points). This velocity is finally transferred onto particle with a formula of the same kind as (4) above :

$$u = \overline{u} * \Lambda : (\mathbb{R}^3 \times \mathbb{R}^3 \times \mathbb{R})^N \equiv \mathbb{R}^{7N} \to \mathcal{C}^k(\mathbb{R}^3)^3 \tag{5}$$

In practice, transfers (4)-(5) plus solving the Poisson equations is faster than evaluating the Biot-Savart formulas (see [4]).

Eventually, the numerical scheme solving the Navier-Stokes equations (1)-(2) with the Lagrangian formalism (3) comes to push particles using a second or fourth order Runge-Kutta scheme to solve the following system of ordinary differential equations :

$$\left\{ \begin{array}{l} \dfrac{\mathrm{d}\omega_p}{\mathrm{d}t} = [\omega \cdot \nabla u](x_p) + \nu \Delta \omega(x_p) \\ \dfrac{\mathrm{d}x_p}{\mathrm{d}t} = u(x_p) \\ \dfrac{\mathrm{d}v_p}{\mathrm{d}t} = \mathrm{div}u(x_p)v_p = 0 \end{array} \right. \tag{6}$$

on a time step, where the stretching $\omega \cdot \nabla u$ is computed on the grid and also transferred to particles by formula (5).

2.2 Time splitting algorithms

In the eighties a technique splitting apart convection and diffusion (see [9]) has appeared to well adapted for flow computation since it separates the difficulties coming from hyperbolic and parabolic parts of the Navier-Stokes equations.

One focuses on solving (6) over a time step. This technique, in the present Lagrangian context, consists in solving successively the hyperbolic convection problem

$$\left\{ \begin{array}{l} \dfrac{\mathrm{d}\omega_p}{\mathrm{d}t} = [\omega \cdot \nabla u](x_p) \\ \dfrac{\mathrm{d}x_p}{\mathrm{d}t} = u(x_p) \end{array} \right. \tag{7}$$

where the velocity field satisfies conditions (2) of no divergence and no-slip-through, and the parabolic diffusion problem

$$\left\{ \begin{array}{l} \dfrac{\mathrm{d}\omega_p}{\mathrm{d}t} - \nu \Delta \omega(x_p) = 0 \\ \dfrac{\mathrm{d}x_p}{\mathrm{d}t} = 0 \end{array} \right. \tag{8}$$

whose initial conditions are the values obtained at the end of the time step by equation (7).

The velocity at boundary, if it exists, vanishes by the full no-slip condition $u = 0$. This takes into account that boundary layers are naturally viscous effects. The treatment of these kinematic boundary conditions is performed by means of a panel method (see [8]), with direct a priori estimates of density (see section 6).

Finally the sum of solutions of (7) and (8) is a first order in time approximation of the solution of (6) at the end of the time step. Second order approximation can be easily obtained (see [2]), but the impact of this first order splitting algorithm has never been restrictive, even for complex flow computations (see [14, 15]).

As any particle method, Vortex in Cell methods requires an distribution of particles as homogeneous as possible in order to avoid both accumulation points and hole of data (that is to say any extreme behavior of particle density). Hence a frequent remeshing process is performed on the particle lattice, that interpolates their values and rearranges it into a uniform lattice, in the spirit of transfer formulae (4) and (5).

Consequently, one can either remesh between solving equation (7) and equation (8) and then begin to solve the parabolic diffusion equation with a uniform lattice, or remesh the particle lattice outside the time evolution algorithm, and then having a fully non-uniformly distributed set of particles. In the first case, a pure finite differences scheme is sufficient to solve the diffusion equation. In the second case, a fully Lagrangian scheme, as accurate as possible, has to be introduced in order solve equation (8).

For flexibility and accuracy considerations, it is thus interesting to build a scheme that has a comparable accuracy with usual finite differences schemes when used on a grid (and presenting also a comparable computational cost), and being more accurate than standard particle strength exchange scheme on particle lattices in a full Lagrangian context. Flexibility is useful in the sense that one scheme can be used with a part of the particles being dispatched on a grid and another part evolving in a non-bounded domain (useful to ensure exact far field conditions), or using the Lagrangian formalism as a local refinement technique.

2.3 Discretization of the diffusion process

Let f be a function solution of the following diffusion equation :

$$\frac{\partial f}{\partial t} - \nu \mathrm{div}(\mathbf{L}\,\nabla f) = 0$$

where the diffusion operator can be written under the form

$$\mathrm{div}(\mathbf{L}\,\nabla f)(x) = \sum_{i,j} \frac{\partial}{\partial x_i}\left(L_{ij}(x)\frac{\partial f}{\partial x_j}\right) \tag{9}$$

which does not depend on time, in order to simplify notations in the current analysis.

One considers a n-particle approximation of function f

$$f^h = \sum_{i=1}^{n} f_i\, v_i\, \delta_{x_i} \quad \text{where} \quad f_i = f(x_i) \tag{10}$$

where h is the characteristic distance between particles (see [7] for instance), and an approximation of the diffusion operator (9) :

$$Q^\varepsilon \cdot f(x) = \int_\Omega \sigma^\varepsilon(x,y)\,\big(f(y) - f(x)\big)\; dy \tag{11}$$

which can be written in its duality form with $Q^\varepsilon \cdot f(x) = \big\langle f - f(x),\, \sigma^\varepsilon(x,\cdot)\big\rangle_{\mathcal{D}'(\Omega),\mathcal{D}(\Omega)}$

Such a particle approximation, called *Particle Strength Exchange* or PSE, leads to the quadrature formula :

$$Q^\varepsilon \cdot f^h(x_k) = \sum_{l=1}^{n} \sigma^\varepsilon(x_k,x_l)\,\big(f_l - f_k\big)\; v_l \tag{12}$$

The goal is to exhibit the relation between the kernel σ^ε of equation (11) and the diffusion matrix $\mathbf{L}$ in equation (9), in order to make formula (12) operational. The classical approach of [7] in three dimensions is summarized in section 2.4, while the discrete formulation is explained in section 3.

2.4 Classical formulation of PSE methods

In this section, one summarizes the method given in [7] in order to get the relation between σ^ε and $\mathbf{L}$.

The diffusion kernel σ^ε, in the spherically symmetric formulation, can be written

$$\sigma^\varepsilon(x,y) = \frac{1}{\varepsilon^7}\,\Theta\left(\frac{y-x}{\varepsilon}\right)\,\mathbf{M}(x,y) : (x-y)^{\otimes 2} \tag{13}$$

which also reads

$$\sigma^\varepsilon(x,y) = \frac{1}{\varepsilon^{2+3+2}}\sum_{i,j=1}^{3}\mathbf{M}_{ij}(x,y)\,(x-y)_i\,(x-y)_j\,\Theta\left(\frac{y-x}{\varepsilon}\right) \tag{14}$$

where Θ, called herein the stencil generator, is a smooth spherical-symmetric function, with fast decreasing, typically such as

$$\Theta(x) = \frac{1}{1+|x|^q}$$

where $|\cdot|$ denotes the Euclidean norm in $\mathbb{R}^3$. Note that one should multiply this function by a smooth partition of unity in order to provide a compact supported function in $\mathcal{D}(\Omega)$ and to be consistent with the dual formulation shown above. Anyway, in practice, only a finite neighborhood is considered in these sums, so the partition of unity is naturally introduced and acts as a cut-off filter, and the dual formulation still holds.

It remains to find the relation between $\mathbf{M}$, Θ and $\mathbf{L}$, which would define the kernel σ^ε and consequently the diffusion operator Q^ε.

A usual approach is to consider the matrix $\mathbf{M}_{ij}(x,y)$ under the form

$$\mathbf{M}_{ij}(x,y) = m_{ij}\left(\frac{x+y}{2}\right)$$

where the matrix $\mathbf{m}(x)$ depends only on one variable. The matrix $A = (a_{kl})$ of second moments of Θ is also introduced :

$$a_{kl} = \int_{\mathbb{R}^3} x_k^2 x_l^2 \Theta(x)\,dx \qquad k,l = 1..3 \tag{15}$$

A fundamental result of [7] is that (12) is a second-order approximation of (9) when the following conditions are satisfied :

$$\begin{cases} m_{kl}(x) = (a_{kl})^{-1} L_{kl}(x) & \text{for } k,l = 1..3,\ k \neq l \\ \\ \displaystyle\sum_{i=1}^{3} a_{ki}\, m_{ii}(x) = 2L_{kk}(x) & \text{for } k = 1..3 \end{cases} \tag{16}$$

If, for $\Theta(x) = \widetilde{\Theta}(|x|)$ (*i*.e. for a spherical-symmetric funtion Θ), one defines the coefficient γ by

$$\gamma = \frac{4\pi}{15}\int_0^{+\infty}\widetilde{\Theta}(r) r^6\,dr$$

Then $a_{kk} = 3\gamma$ and $a_{kl} = \gamma$ for $k \neq l$. The solution of problem (16) is then explicitly given by

$$m_{kl} = \gamma^{-1} L_{kl} \qquad et \qquad m_{kk} = \gamma^{-1} L_{kk} - \frac{\gamma^{-1}}{5} \operatorname{Tr}(\mathbf{L})$$

thus finally

$$\mathbf{m} = \gamma^{-1}\mathbf{L} - \frac{\gamma^{-1}}{5} \operatorname{Tr}(\mathbf{L})\mathbf{Id_3} \tag{17}$$

Equation (17) is the conclusion since $\mathbf{m}$ gives a construction of $\mathbf{M}$, thus of σ^ε and finally of Q^ε. The numerical scheme (12) is then well-defined.

Furthermore, one may notice that if $\Theta(x) = (1 + \|x\|^{14})^{-1}$, there is an easy computation of γ :

$$\gamma = \frac{4\pi}{15} \int_0^{+\infty} \frac{r^6}{1 + r^{14}}\, dr = \frac{4\pi}{15} \left[\frac{1}{7} \arctan\left(r^7\right) \right]_0^{+\infty} = \frac{2\pi^2}{105}$$

One can notice that γ^{-1} can be factorized in equation (17), and consequently γ can be tuned in order to gain accuracy after a measurement of dissipation errors. An other way to proceed, which does not involve tuning, is to re-establish these formula in a discrete formulation. The next section will show that two integral parameters γ_1 and γ_2 are actually involved when rebuilding the formulas, and will lead to a more complex but more accurate numerical scheme.

3 Discrete Particle Strength Exchange scheme

The classical theory of PSE methods described above has been proved to be second order consistent in the sense $h/\varepsilon \to 0$, that is to say the error is $\mathcal{O}[(h/\varepsilon)^2]$. This formulation is valid for arbitrary distribution of particles, and its accuracy can be improved by taking a larger diffusion kernel width ε. Nevertheless, engineering concerns lead to chose usually h/ε constant in order to take in account strong variation of the solution from a particle to its neighborhood (thus the necessity to avoid large stencil). This fact is especially important for large three-dimensional direct numerical simulations that are often to the limit of under-resolution.

This section focuses on a kind of renormalization of the particle strength exchange scheme when particle are distributed over a uniform grid (or a mapping thereof). We will show that the renormalized scheme comes to be fully second order consistent as $\mathcal{O}[h^2]$ instead of $\mathcal{O}[(h/\varepsilon)^2]$.

Indeed, when particles are dispatched on a uniform grid (in mapped coordinates, the stretching being provided by the operator $\mathbf{L}$, for example cylindrical or spherical coordinates), one can introduce a discrete evaluation of integral (15), that is to say the matrix of discrete second order moments of kernel Θ :

$$a_{kl} = \sum_{x \in h\mathbb{Z}^3} x_k^2 x_l^2 \Theta(x) h^3 \quad \text{for} \quad k, l = 1..3 \tag{18}$$

Using discrete integration allows more compatibility between summations in (12) and leads to a more conservative scheme, hence a gain of accuracy. But the loss of continuity breaks the relation $a_{kk} = 3a_{kl} = 3\gamma$, and relation (17) does not hold anymore. In the following section 3.1 one builds a discrete scheme based on discrete integration and one takes into account this loss of symmetry. Then, in section 3.3, one will exhibit convergence rate on a benchmark.

3.1 Discrete formulation

In order to give a sense to discrete computations and find a formulation in the same spirit of (17), one introduces the coefficients

$$\begin{cases} \gamma_1 = \displaystyle\sum_{x\in h\mathbb{Z}^3} x_k^4 \Theta(x) h^3 \\ \\ \gamma_2 = \displaystyle\sum_{x\in h\mathbb{Z}^3} x_k^2 x_l^2 \Theta(x) h^3 \end{cases}$$

Thus $\gamma_1 \neq 3\gamma_2$, and the matrix A is then given by :

$$A = \begin{bmatrix} \gamma_1 & \gamma_2 & \gamma_2 \\ \gamma_2 & \gamma_1 & \gamma_2 \\ \gamma_2 & \gamma_2 & \gamma_1 \end{bmatrix}$$

The first relation of (16) reads

$$m_{kl}(x) = a_{kl}^{-1} L_{kl}(x) = \frac{1}{\gamma_2} L_{kl}(x) \quad \text{for} \quad k,l = 1..3,\ k \neq l \tag{19}$$

One can thus define a vector for diagonal components of $\mathbf{m}$, as $\widetilde{m}_k = m_{kk}$ and $\widetilde{L}_k = L_{kk}$.

The second relation of (16) reads $A\widetilde{m} = 2\widetilde{L}$ which means $\widetilde{m} = 2A^{-1}\widetilde{L}$.

One gets $\det A = \gamma_1^3 - 3\gamma_1\gamma_2^2 + 2\gamma_2^3$ and

$$A^{-1} = \frac{1}{\gamma_1^2 + \gamma_1\gamma_2 - 2\gamma_2^2} \begin{bmatrix} \gamma_1+\gamma_2 & -\gamma_2 & -\gamma_2 \\ -\gamma_2 & \gamma_1+\gamma_2 & -\gamma_2 \\ -\gamma_2 & -\gamma_2 & \gamma_1+\gamma_2 \end{bmatrix}$$

Let $\mathbf{F}$ be the matrix whose coefficients are all equal to 1. The last expression then reads :

$$A^{-1} = \frac{1}{\gamma_1^2 + \gamma_1\gamma_2 - 2\gamma_2^2} \left((\gamma_1 + 2\gamma_2)\mathbf{Id_3} - \gamma_2 \mathbf{F} \right)$$

thus

$$\widetilde{m} = \frac{2(\gamma_1+2\gamma_2)}{\gamma_1^2 + \gamma_1\gamma_2 - 2\gamma_2^2} \widetilde{L} - \frac{2\gamma_2}{\gamma_1^2 + \gamma_1\gamma_2 - 2\gamma_2^2} \mathbf{F}\, \widetilde{L}$$

One can notice that vector $\mathbf{F}\,\widetilde{L}$ has all its components equal to $\mathrm{Tr}\mathbf{L}$. Consequently, one gets a relation similar to (16) which is consistent with discret integration :

$$m_{kk} = \frac{2(\gamma_1+2\gamma_2)}{\gamma_1^2 + \gamma_1\gamma_2 - 2\gamma_2^2} L_{kk} - \frac{2\gamma_2}{\gamma_1^2 + \gamma_1\gamma_2 - 2\gamma_2^2} \mathrm{Tr}\mathbf{L} \tag{20}$$

In order to write this in a compact and matrix formulation, one has to introduce the matrix $\mathbf{H} = H_{ij}$

$$H_{ij} = \left(\frac{\gamma_1^2 - \gamma_1\gamma_2 - 6\gamma_2^2}{\gamma_2(\gamma_1^2 + \gamma_1\gamma_2 - 2\gamma_2^2)} \right) (1 - \delta_{ij})\, L_{ij} \tag{21}$$

where δ_{ij} is the Kronecker symbol. This matrix $\mathbf{H}$ is zero when $\mathbf{L}$ is diagonal or when $\gamma_1 = 3\gamma_2$ (*i*.e. in the continuous case).

Finally, relations (19) and (20) can be written in the same spirit of (16) as

$$\mathbf{m} = \frac{2(\gamma_1+2\gamma_2)}{\gamma_1^2 + \gamma_1\gamma_2 - 2\gamma_2^2} \mathbf{L} \ - \ \frac{2\gamma_2}{\gamma_1^2 + \gamma_1\gamma_2 - 2\gamma_2^2} \mathrm{Tr}(\mathbf{L})\mathbf{Id_3} \ + \ \mathbf{H} \tag{22}$$

Furthermore, $\gamma_1 = 3\gamma + \mathcal{O}(h)$ and $\gamma_2 = \gamma + \mathcal{O}(h)$, which implies that $\mathbf{H} = \mathcal{O}(h)$, thus $\mathbf{m}$ of equation (22) satisfies

$$\mathbf{m} = \gamma^{-1}\mathbf{L} - \frac{\gamma^{-1}}{5}\operatorname{Tr}(\mathbf{L})\mathbf{Id_3} + \mathcal{O}(h) \tag{23}$$

The discrete formulation is thus at least a first order approximation of the classical scheme, but is intrinsically second order, fact discussed in next section.

3.2 PSE scheme in Cartesian coordinates

The stencil chosen to study convergence is under the form $\Theta(x) = (1 + |x|^p)^{-1}$ where $|\cdot|$ is the Euclidean norm in $\mathbb{R}^3$, which leads to

$$\gamma = \frac{4\pi}{15}\int_0^{+\infty} \Theta(r) r^6 \,\mathrm{d}r = \frac{4\pi^2}{15n\,\sin(7\pi/n)}$$

and gives, for our choice $p = 10$, the value $\gamma = 0.32532$. For the computation of discrete moments, one chooses the one-particle neighborhood, which gives a kernel cut-off value of $\Theta(2) = 9.756\,10^{-4}$.

One considers a sub-lattice $\mathbb{J}$ of the three-dimensional lattice $h\mathbb{Z}^3$ whose knots are uniformly distributed. The points $x \in \mathbb{J}$ are indexed in a set of indexes $\mathbb{I}$ (this means $x_k \in \mathbb{J}$ with $k \in \mathbb{I}$). This gives the particle estimation of a function f as

$$P_h f = \sum_{x\in\mathbb{J}} f(x)\delta_x h^3$$

which can be described itself intrinsically as a measure function

$$f^h = \sum_{k\in\mathbb{I}} f_k \delta_{x_k} v_k$$

where h is the characteristic length between knots of the lattice $\mathbb{J}$, each point x_k being associated to a volume $v_k = h^3$ and a value $f_k = f(x_k)$.

The PSE scheme, that is to say the evaluation of the Laplacian of f^h, reads

$$Q^\varepsilon \cdot f^h(x_k) = \frac{1}{\varepsilon^7}\sum_{l\sim k} \frac{f_l - f_k}{1 + \left|\frac{x_l - x_k}{\varepsilon}\right|^p}\left[\sum_{i,j=1}^{3} m_{ij}\left(\frac{x_l + x_k}{2}\right)(x_l - x_k)_i (x_l - x_k)_j\right] v_l \tag{24}$$

where the sum over $l \sim k$ means the sum over particles of index l in the 1-neighborhood of particle of index k in the lattice $\mathbb{J} \subset h\mathbb{Z}^3$.

In Cartesian coordinates, on has $\mathbf{L} = \mathbf{Id_3}$, and $\operatorname{div}(\mathbf{L}\nabla f) = \Delta f$, and consequently the matrix $\mathbf{m}$ is given, respectively for the continuous (standard) case and the discrete case, by

$$\mathbf{m} = \frac{2}{5\gamma}\mathbf{Id_3} \quad \text{and} \quad \mathbf{m} = 2\frac{\gamma_1 - \gamma_2}{\gamma_1^2 + \gamma_1\gamma_2 - 2\gamma_2^2}\mathbf{Id_3} \tag{25}$$

Since in both these cases the matrix $\mathbf{m}$ is diagonal with constant coefficients, the scheme (24) reads

$$Q^\varepsilon \cdot f^h(x_k) = \frac{\alpha}{\varepsilon^7}\sum_{l\sim k} \frac{|x_l - x_k|^2}{1 + \left|\frac{x_l - x_k}{\varepsilon}\right|^p}(f_l - f_k)v_l \tag{26}$$

where α is the diagonal coefficient of $\mathbf{m}$ and $|\cdot|$ the Euclidean norm in $\mathbb{R}^3$.

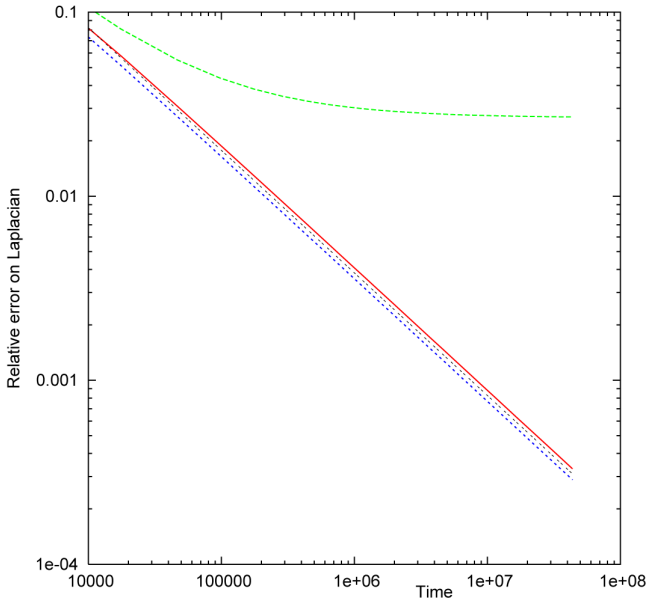

Figure 1: Second order convergence of Discrete PSE scheme (red) for a Gaussian scalar function : error in shown to be of order h^2 with h/ε constant, compared to standard PSE (green), and standard 7 points centered finite difference scheme (blue). Dashed black line is $n^{-2/3}$, n being the number of grid points.

3.3 Numerical convergence of the discrete scheme

One considers as a first benchmark a spherical Gaussian scalar blob

$$f(x) = \frac{1}{(2\pi\sigma^2)^{3/2}} e^{-x^2/2\sigma^2} \tag{27}$$

with $x \in \mathbb{R}^3$, whose isovalues are concentric spheres. This function satisfies

$$\Delta f(x) = \left(\frac{x^2}{\sigma^2} - 3\right) \frac{f(x)}{\sigma^2}$$

To exhibit convergence rate one considers the $\mathbb{L}^2$ relative error defined by

$$\frac{\|Q^\varepsilon P_h f - P_h \Delta f\|_2}{\|P_h \Delta f\|_2} = \left(\frac{\sum_{x\in\mathbb{J}} \left(Q^\varepsilon P_h f(x) - \Delta f(x)\right)^2 h^3}{\sum_{x\in\mathbb{J}} \Delta f(x)^2 h^3} \right)^{1/2} \tag{28}$$

One uses the computational domain $[-3,3]^3$ with several discretizations of grid size $N \times N \times N$ containing thus $n = N^3$ points, with a grid step $h = 6/N = 6n^{-1/3}$. the standard deviation of the blob is chosen as $\sigma = 1/2$, and the PSE kernel width locked on the grid step $\varepsilon = h$, which should prevent the standard PSE scheme from converging since its error is of order $(h/\varepsilon)^2$.

On figure 1 is plotted the $\mathbb{L}^2$ relative error on Δf with respect to the number of grid points n, and shows that the Discrete PSE scheme is of order 2, that is to say converges as h^2 (or equivalently $n^{-2/3}$), with the same rate of the standard 7 points finite difference scheme also plotted on this figure. Moreover, as expected the standard PSE does not converges since h/ε is constant.

One will now show that it can provide a gain of accuracy for three-dimensional flow computations, with or without the presence of boundary layers.

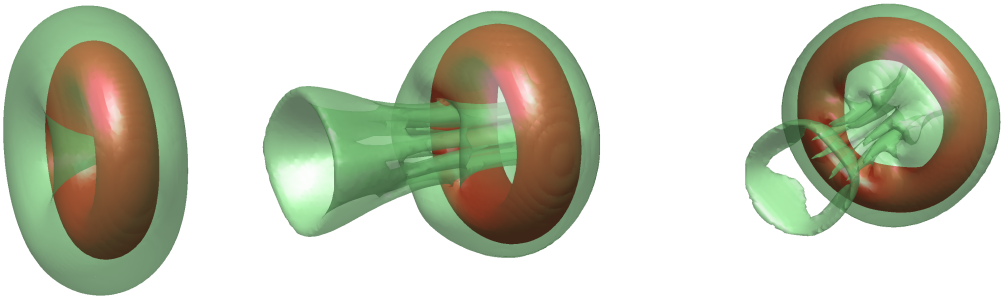

Figure 2: Surfaces of isovorticity of ω^2 (red at 10^{-1} and green at 10^{-3}) of a vortical ring at different times (left to right 0, 50, 60) for a Reynolds number $Re = 2000$.

4 Vortical rings

One considers, in the coordinates (x, y, z), a vortical ring of axis e_x, which depends on several parameters : its strength Γ, the distance α between the ring center and the origin, a radius R and a standard deviation σ. Posing $\phi(x, y, z) = -\sqrt{y^2 + z^2}$, $e_\phi = \mathrm{curl}[\phi(x, y, z)e_x]$ and

$$\rho(x, y, z) = (R + \phi)^2 + (x - \alpha)^2$$

one considers the vorticity field given by $\omega = \omega_\phi e_\phi$ with

$$\omega_\phi(x, y, z) = \frac{\Gamma}{2\pi\sigma^2} e^{-\rho(x,y,z)/2\sigma^2} e_\phi$$

Furthermore, the vectorial Laplacian in cylindrical coordinates (x, r, ϕ) is given by

$$\begin{cases} e_r \cdot \Delta\omega = \Delta\omega_r - \dfrac{\omega_r}{r^2} - \dfrac{2}{r^2}\dfrac{\partial\omega_\phi}{\partial\phi} \\ e_\phi \cdot \Delta\omega = \Delta\omega_\phi - \dfrac{\omega_\phi}{r^2} + \dfrac{2}{r^2}\dfrac{\partial\omega_r}{\partial\phi} \\ e_x \cdot \Delta\omega = \Delta\omega_x \end{cases}$$

Since for vortical ring defined above, components ω_r and ω_x are identically equal to zero and ω_ϕ is independent of ϕ, one gets

$$\Delta\omega = \left(\Delta\omega_\phi - \frac{\omega_\phi}{r^2}\right) e_\phi = \left(\frac{\rho}{\sigma^4} - \frac{2}{\sigma^2} - \frac{1}{r^2} + \frac{\beta - r}{r\sigma^2}\right) \omega \tag{29}$$

One can immediately notice that the singularity in r^{-2} is stronger when ω_ϕ has a large value at $r = \sqrt{y^2 + z^2} = 0$, that is to say when β is small. This phenomena is shown on figure 3 on which are plotted contours of two vortical rings and their Laplacian for two core radius $\beta = 1.4$ and $\beta = 2$, other parameters being set to $\alpha = 0$ and $\Gamma = 1$ in the box $\Omega = [-2\pi, 2\pi]^3$.

These two rings provide two other benchmarks to study convergence rate. Indeed, one proceeds as in last section for the scalar Gaussian function : the box is discretized into a grid $N \times N \times N$ containing $n = N^3$ points with a grid step $h = 2\pi\, n^{-3}$. One can then compare the difference between the exact value of Δw and the numerical solution obtained by the standard PSE (which does not converges since h/ε does not tends to zero), the discrete PSE and the standard 7 points finite differences scheme.

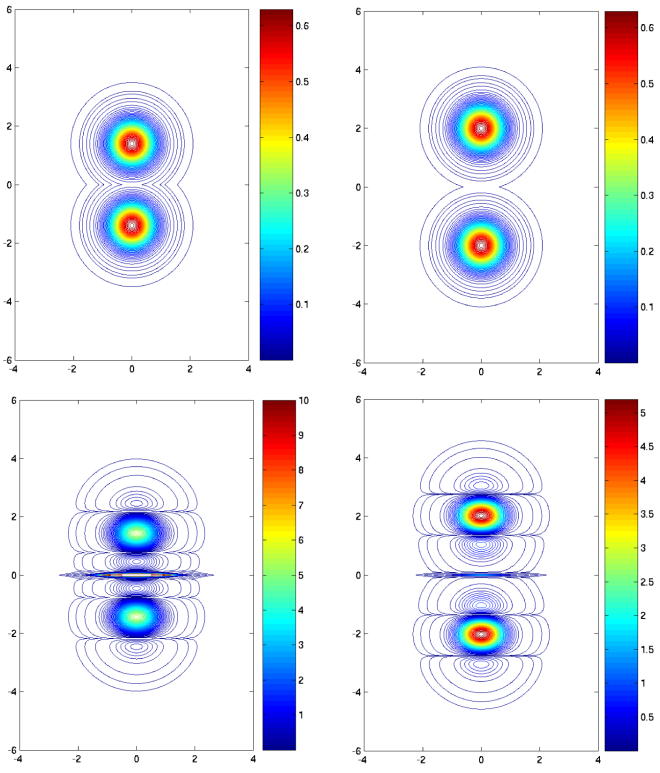

Figure 3: Contours of $\|\omega\|$ (top) and $\|\Delta\omega\|$ (bottom) in the slice $y = 0$ of vortical rings for two core radius $\beta = 1.4$ (left) and $\beta = 2$ (right). $\Delta\omega$ exhibits a stronger singularity for smaller core radius (bottom left).

These comparisons are provided on figure 4, one which one can see that both Discrete PSE and finite differences converges as h^2 without noticing the singularity in the case of a large core radius $\beta = 2$ (left picture).

Furthermore, when the singularity becomes stronger in the case of a smaller core radius $\beta = 1.4$, then the finite difference scheme tends to give an error which is an order or magnitude higher than discrete PSE. This comes from the fact that the whole neighborhood is involved in the computation of the diffusion, while usual finite difference schemes use only points on axis around the base point.

This feature of PSE schemes is especially interesting when large variation of vorticity are present in the flow or in neighborhood of hyperbolic points which are numerous in wakes for example (see [15]).

The dynamic of these rings and thus the behavior of conservation laws using these schemes when several grid sizes will now be discussed. The Reynolds number for tubular shaped vortex structures is commonly defined by $Re = \Gamma/\nu$. At low Reynolds numbers, the typical dynamics of these rings is purely translative until diffusion reduce enstrophy sufficiently to reach a steady position where the ring finishes to diffuse. At higher Reynolds numbers, a tail and vortex dislocation can appear, as shown on figure 2 at $Re = 2000$, which provides a non-trivial benchmark to carry out dissipation rates. The parameters used herein are $\alpha = 4$, $R = 1.4$, $\Gamma = 1$ and $\nu = 1/2000$, in the box $\Omega = [-2\pi,\, 2\pi]^3$.

The usual law followed by the kinetic energy is

$$\frac{dE}{dt} = -\nu Z \tag{30}$$

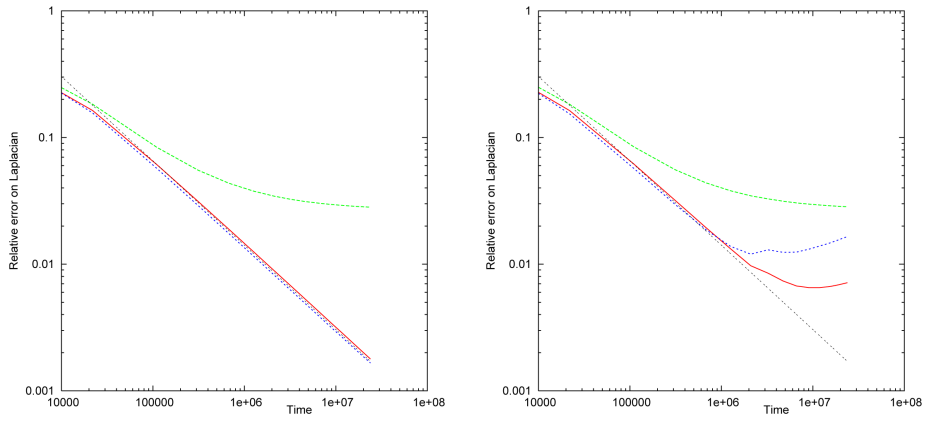

Figure 4: Convergence of Discrete PSE scheme (red) for two vortical rings (large core radius $\beta = 2$ on left picture and small core radius $\beta = 1.4$ on right picture) : $\mathbb{L}^2$ error with respect to the number of grid points $n = h^{-1/3}$ compared to standard PSE (green), and standard 7 points centered finite difference scheme (blue). Dashed black line is $n^{-2/3}$.

where Z is the enstrophy and E the kinetic energy, given respectively by

$$Z = \int_\Omega \omega^2(x)\,dx = \|\omega\|^2_{2,\Omega} \quad \text{and} \quad E = \frac{1}{2}\int_\Omega u^2(x)\,dx = \frac{1}{2}\|u\|^2_{2,\Omega}$$

Hence the introduction of numerical estimation of viscosity, called effective viscosity, based on numerical values of energy and enstrophy, defined by

$$\nu_{\text{eff}} = -\frac{1}{Z}\frac{dE}{dt} \tag{31}$$

This diagnostic (31) is difficult to manage due to small divisor δt when computed numerically, and also since Z tends to 0 for large times, which is specially significant at low Reynolds numbers because of fast diffusion.

5 Random vortical blob

For this study one will consider initially a Gaussian blob of random field of vorticity, built as follows. Lets X_1, X_2 and X_3 be three independent and dimensionless random real variables following a centered Gaussian law $\mathcal{N}(0,\sigma)$ of standard deviation σ. These Gaussian variables X_i are generated by the usual Box-Muller method, that is to say if Y and Z are two independent random variables following a uniform law on $[0,1]$ (which is obvious to implement), then

$$X = \sigma\sqrt{-2\ln Y}\,\cos(2\pi Z)$$

follows the centered Gaussian law $\mathcal{N}(0,\sigma)$.

One defines the vectorial random variable $W = 3^{-1/2}(X_1, X_2, X_3)$ whose square has the expectation

$$\mathbb{E}[W^2] = \frac{1}{3}\sum_{i=1}^{3}\mathbb{E}[X_i^2] = \sigma^2$$

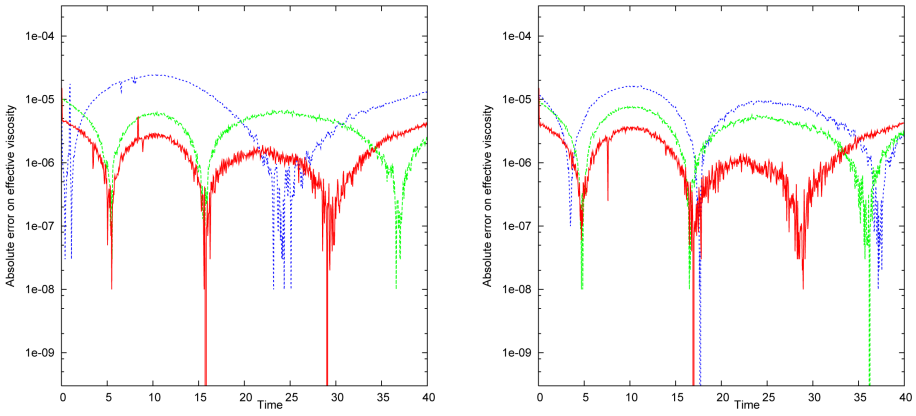

Figure 5: Absolute error on effective viscosity with respect to time of discrete PSE scheme (to the left) and standard finite difference scheme (to the right) for the flow generated by a vortical ring, at resolutions 96^3 (blue), 128^3 (green) and 192^3 (red) and $Re = 1000$.

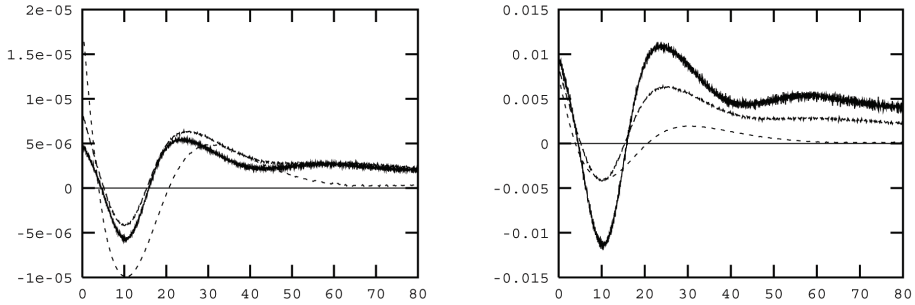

Figure 6: Effective viscosity ν_{eff} versus time, for several Reynolds numbers, of a flow created by a vortical ring in periodical domain using discrete formulation of PSE scheme and a resolution 128^3. Left picture is absolute error and right picture is relative error (—— $Re = 2000$, – – – $Re = 1000$, - - - - $Re = 400$).

and then the following random field of vorticity $\omega(\xi)$ of strength Γ, with $\xi \in \mathbb{R}^3$, by

$$\overline{\omega}(\xi) = \Gamma\, W(\xi)\, \frac{e^{-\xi^2/2s^2}}{(2\pi s^2)^{3/2}}$$

The associated Reynolds number based on circulation in the quadratic meaning is defined as

$$Re = \frac{\left\langle \mathbb{E}[\overline{\omega}(\xi)^2]^{1/2} \right\rangle}{\nu} = \frac{1}{\nu} \int_{\mathbb{R}^3} \mathbb{E}\left[\, \overline{\omega}(\xi)^2 \,\right]^{1/2} \mathrm{d}\xi = \frac{\Gamma\, \sigma}{\nu}$$

Moreover, this vorticity field has no reason to be divergence free so one proceeds to the projection $\omega = \mathrm{curl}^2 \Delta^{-1} \overline{\omega}$ on divergence-free fields. The dynamics of such a flow is qualitatively given by surfaces of isovorticity, plotted of figure 7 for $\Gamma = 1.7$, $\sigma = 1$, $s = 1$ and $\nu = 1/2000$, which leads to $Re = 2000$, with a time step $\delta t = 0.1$. Figure 9 also exhibits the surfaces of isovorticity obtained for the same parameters unless $\Gamma = 170$, which gives $Re = 2\,10^5$ and leads to a much shaky evolution.

The main analysis that can be carried out from these simulations is that the effective viscosity, plotted on figure 8 for the two Reynolds numbers mentioned above, is always closer to the theoretical viscosity than the standard PSE scheme, but in a much less sensible manner than for flows

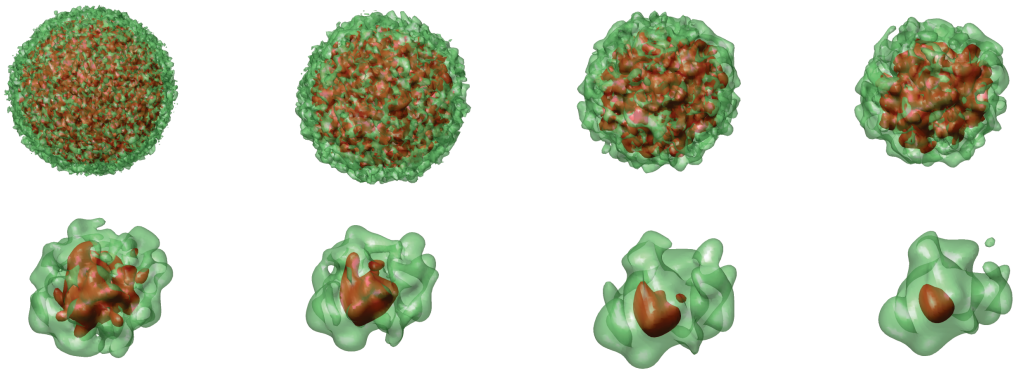

Figure 7: Surfaces of isovorticity of ω^2 (red at 10^{-3} and green at 10^{-4}) of a random spherical blob of vorticity at different times (left to right and top to bottom at 0, 2, 6, 10, 20, 30, 40 and 50) for a Reynolds number $Re = 2\,10^3$ (with $\Gamma = 1.7$).

which do not involve small scale structures, such as the vortical rings described in last section. Furthermore, one can also notice that the improved PSE scheme has no significant effect of energy spectra, as shown on figure 10 for a Reynolds number $Re = 2000$. One also notice on this figure the development of a short inertial range featuring the power law $k^{-5/3}$.

6 Flow around a cylinder

In the previous sections, one has considered flows in Cartesian coordinates without any physical boundary on which there would be no-slip conditions. One now considers the case of a vortical ring moving toward a cylindrical body on which is created a boundary layer. The strong interaction between the main ring and the boundary layer creates successively a secondary ring that quits the boundary layers to reconnect to the main vortical structure. The dynamic is qualitatively represented on figure 11 by surfaces of isovorticity.

The cylindrical coordinates induce an anisotropic diffusion operation in mapped coordinates (r, θ, z). Indeed, the diffusion equation reads

$$\frac{\partial \omega}{\partial t} - \frac{\nu}{r}\mathrm{div}(\mathbf{L}\,\nabla\omega) = 0 \tag{32}$$

where $\mathrm{div}(\mathbf{L}\,\nabla\omega) = r\Delta\omega$ and

$$\mathbf{L}(r,\theta,z) = \begin{bmatrix} r & 0 & 0 \\ 0 & 1/r & 0 \\ 0 & 0 & r \end{bmatrix}$$

whose condition at boundaries is of kinematic type, that is to say $u = \mathrm{curl}\Delta^{-1}\omega = \mathrm{curl}\Psi = 0$, and its initial condition ω_0 being the vorticity field obtained at the end of the convection step, developped in sections 2.1 and 2.2 (see [5] or [6] for more details on this algorithm).

In this case the trace of operator $\mathbf{L}$ is no longer constant and the PSE schemes (standard or discrete) given by formula (24) cannot be written as simply as in Cartesian coordinates, that is to say formula (25). Nevertheless, diffusion operator $\mathbf{L}$ is diagonal, and consequently matrix H defined in formula (21) is zero.

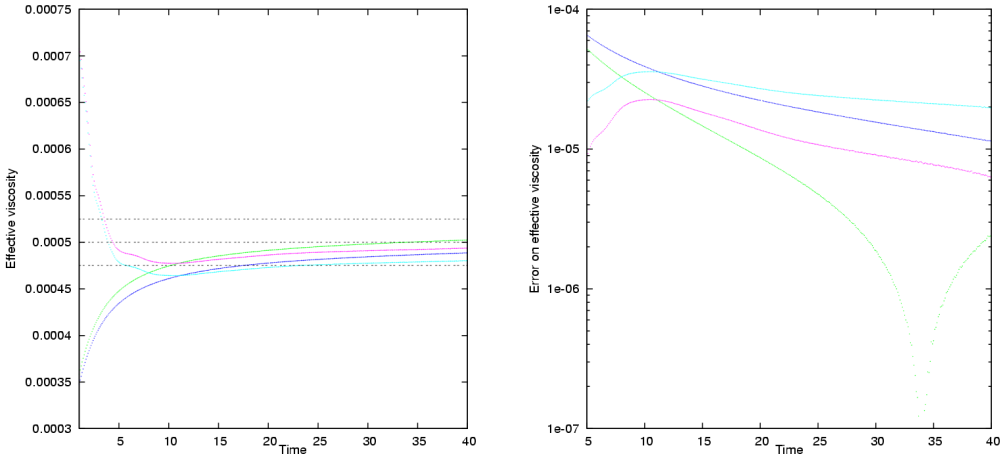

Figure 8: Effective viscosity (left picture) and absolute error with theoretical viscosity (right picture) for a random vortical field at Reynolds numbers $Re = 2\,10^3$ (standard PSE is dark blue, improved PSE is green) and $Re = 2\,10^5$ (standard PSE is cyan, improved PSE is magenta). Black dashed lines on left picture indicates the theoretical viscosity $\nu = 5\,10^{-4}$ and $\pm 5\%$ deviation level.

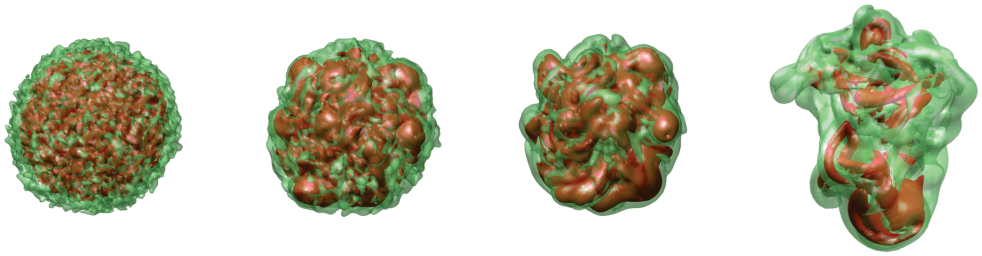

Figure 9: Surfaces of isovorticity of ω^2 (red at 10^{-1} and green at 10^{-2}) of a random spherical blob of vorticity at different times (left to right at 2, 6, 12 and 24) for a Reynolds number $Re = 2\,10^5$ (with $\Gamma = 170$).

The PSE scheme (24) can be written, in mapped coordinates $\overline{x} = (r, \theta, z)$ of physical point $x = (r\cos\theta, r\sin\theta, z)$, as

$$Q^\varepsilon \cdot f^h(\overline{x}_k) = \frac{1}{\varepsilon^7} \sum_{l \sim k} \frac{f_l - f_k}{1 + \left|\frac{\overline{x}_l - \overline{x}_k}{\varepsilon}\right|^p} \left[\sum_{i=1}^{3} m_{ii} \left(\frac{r_l + r_k}{2} \right) \left[(\overline{x}_l - \overline{x}_k)_i \right]^2 \right] v_l \qquad (33)$$

where coefficients m_{ii} are given by relation(16), which reads for this diffusion operator :

$$m_{11}(r) = m_{33}(r) = \frac{2}{\gamma_1^2 + \gamma_1\gamma_2 - 2\gamma_2^2} \left(\gamma_1 r - \frac{\gamma_2}{r} \right)$$

and

$$m_{22}(r) = \frac{2}{\gamma_1^2 + \gamma_1\gamma_2 - 2\gamma_2^2} \left(\frac{\gamma_1 + \gamma_2}{r} - 2\gamma_2 r \right)$$

A way to proceed kinematic boundary condition is use Chorin's algorithm, described in the case of three-dimensional circular cylinder in [5]. This consists in splitting equation (32) in two

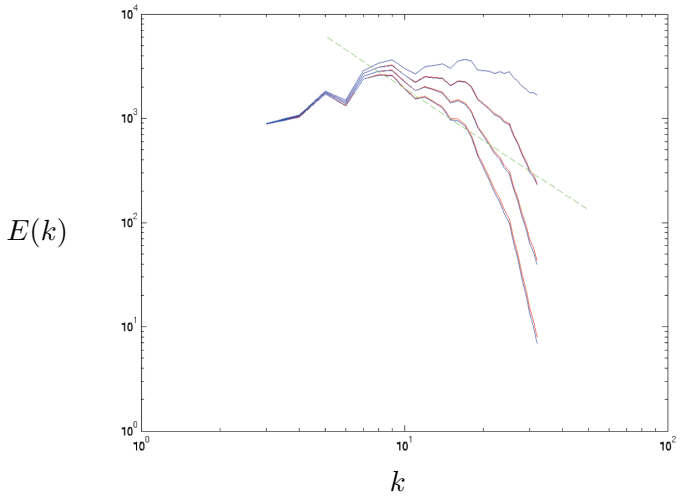

Figure 10: Energy spectra at times $t = 0$, 2, 4 and 6 (top to bottom) for standard (red) and improved (blue) PSE method, at $Re = 2\,10^3$. Green dashed line exhibits $k^{-5/3}$.

parts with Robin-Fourier boundary conditions divergence-free compatible, in this case :

$$\mathcal{T}\omega = \begin{pmatrix} \dfrac{w_r}{r} \\ \dfrac{w_\theta}{r} + \dfrac{\partial w_\theta}{\partial r} \\ \dfrac{\partial w_z}{\partial r} \end{pmatrix} \tag{34}$$

In practice, pure Neumann conditions are often used and can nevertheless lead to nicely accurate results (cf. [13]), especially when Reynolds number increases.

The first part is homogeneous and writes

$$\begin{cases} \dfrac{\partial \omega}{\partial t} - \dfrac{\nu}{r}\mathrm{div}(\mathbf{L}\,\nabla\omega) = 0 \quad in\ \Omega\times]0,T[\\ \nu\mathcal{T}\omega = 0 \quad on\ \partial\Omega\times]0,T[\\ \omega(x,0) = \omega_0(x) \quad on\ \Omega \end{cases} \tag{35}$$

which leads to a vectorial slipping velocity $u_s(t)$ for any time $t \leqslant T$. The second part is non-homogeneous and writes

$$\begin{cases} \dfrac{\partial \omega}{\partial t} - \dfrac{\nu}{r}\mathrm{div}(\mathbf{L}\,\nabla\omega) = 0 \quad in\ \Omega\times]0,T[\\ \nu\mathcal{T}\omega = J\dfrac{\partial u_s}{\partial t} \quad on\ \partial\Omega\times]0,T[\\ \omega(x,0) = 0 \quad on\ \Omega \end{cases} \tag{36}$$

where J is the rotation matrix of angle $\pi/2$ in tangential bundle. The solution of equation (36) has significant value only close to boundary and there exist integral techniques able to solve this equation with a linear complexity, that is to say with a computation time proportional to the boundary lattice number of points (see [10] for examples). The sum of solutions of equations (35) and (36) is then a first order of equation (32) with kinematic boundary conditions (see [2] for instance).

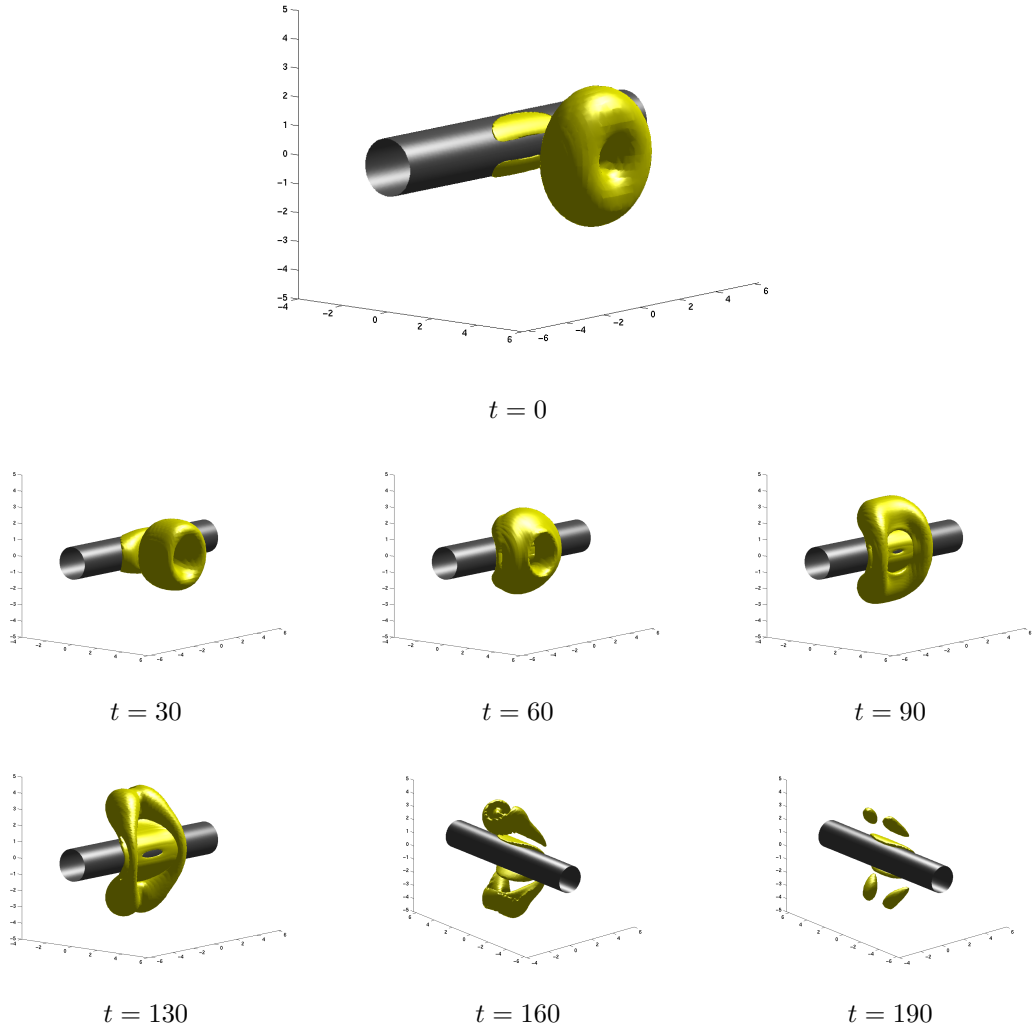

Figure 11: Isovorticity surfaces at different times for a vortical ring self-propulsed on a cylindrical body, and interacting with the boundary layer.

The first part (35) is consequently the step that requires most resources for such a computation, especially since this vectorial heat equation has its components coupled either with the evolution law or at boundaries. A way to run a fast evaluation of its solution is to split it in two again, but this time playing with linearity of the heat equation, thus not introducing any other approximations :

$$\begin{cases} \dfrac{\partial \omega}{\partial t} - \dfrac{\nu}{r}\mathrm{div}(\mathbf{L}\,\nabla\omega) = 0 \quad in\ \Omega\times]0,T[\\ \omega(x,0) = \omega_0(x) \quad on\ \Omega \end{cases} \tag{37}$$

with arbitrary boundary conditions, and whose solution is denoted ω^*.

If the vorticity field ω is itself written in Cartesian coordinates, but its three variables in cylindrical coordinates, equation (37) can be uncoupled in three scalar heat equation and solved using the discrete PSE scheme defined by formula (33), for example joint to an explicit Euler scheme

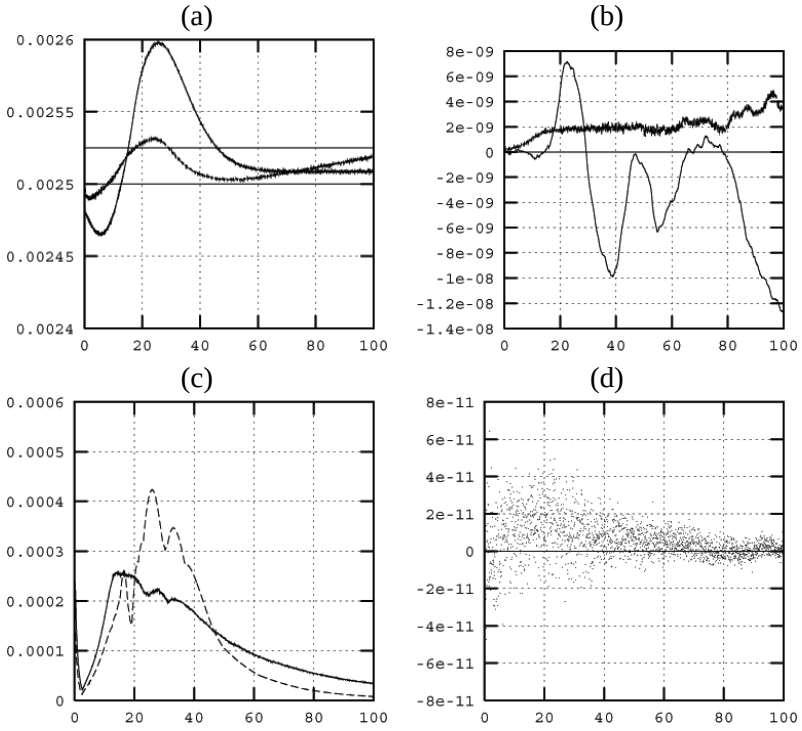

Figure 12: Diagnostics. *From left to right and top to bottom* :
(a) Numerical viscosity (coarse and fine simulations, theoretical values at $1/400$ and $+1\%$),
(b) Global circulations (coarse and fine simulations),
(c) Maximum residual tangential velocity (fine simulation),
(d) Helicity (fine simulation).

(or implicit if viscosity is too high). Note that this is possible only because of the lack of boundary condition, because as defined herein, PSE schemes do not control values of the solution at boundaries (but could be assimilated to be a flux).

In order to enforce homogeneous boundary conditions, one has to consider the following equation :

$$\begin{cases} \dfrac{\partial \omega}{\partial t} - \dfrac{\nu}{r}\mathrm{div}(\mathbf{L}\,\nabla\omega) = 0 \quad in\ \Omega\times]0,T[\\ \nu\mathcal{T}\omega = -\nu\mathcal{T}\omega^* \quad on\ \partial\Omega\times]0,T[\\ \omega(x,0) = 0 \end{cases} \tag{38}$$

One can notice that this equation is of the same kind as equation (36), allowing fast estimations of the solution, and that the sum of solutions of equations (37) and (38) is solution of equation (35) with homogeneous boundary condition. Consequently, the sum of solution of equations (37), (38) and (36) is an approximation of the initial problem (32) with kinematic boundary condition, most computation time being used by the computation of PSE schemes in equation (37) and the estimation of the velocity field u_s after having solved equation (38).

Diagnostics for this simulation of a vortical ring interacting with a cylindrical body are plotted on figure 12. One can notice on this figure that indeed, the no-slip condition is not algebraically satisfied but maximum residual velocity on the body stays small (on graph (c)). The global circulation and helicity are globally conserved accurately, despite the strength and the evolution of the

boundary layer (respectively graphs (b) and (d)).

Furthermore, the kinetic energy conservation law is investigated by means of te effective viscosity ν_{eff} defined and used in previous sections. Only two resolutions were carried out, $64 \times 128 \times 64$ and $128 \times 256 \times 128$, called respectively coarse and fine simulations in legend of figure 12. Indeed, considering coarser grids would give hazardous results while finer grids were not easily manageable on standard computer resources at the time these simulations were done due to the large number of vectorial grids to store (velocity, vorticity, volumes, stream, potential stream, stretching, some of same at any sub-step of the Runge-Kutta scheme for time evolution).

Nevertheless, for these two simulations, one notices that error on effective viscosity is reduced by a factor 4 while the grid step size is reduced by 2, which is compatible with the intrinsically second order of discrete particle exchange scheme. One can conclude that for this kind of simulation, the discrete PSE scheme is once again an accurate tool and one completes the results presented in previous sections in Cartesian coordinates (thus with isotropic diffusion) without physical boundaries by an analysis in cylindrical coordinates (with anisotropic diffusion in mapped coordinates) with a cylindrical body on which one has satisfied numerically the no-slip condition.

7 Sensitivity to perturbation of knot location

One has proved in the last section the renormalized particle strength exchange scheme can be assimilated to a finite difference stencil on uniformly discretized grid, and leads to the same order of accuracy on various problems.

Now one can discuss the advantage of PSE over finite difference schemes. Indeed, the particle strength exchange has been introduced to treat diffusion in a Lagrangian context, where particles are not necessarily dispatched on a grid. One has shown that PSE is not accurate when the support width of diffusion kernel ε is adjusted to the grid step h, to the opposition of its discrete formulation.

One will now focus on the behavior of discrete particle strength exchange scheme when particle are not dispatched on a grid, and compare it to standard PSE. In this case standard centered finite differences are pointless but are computed anyway to carry out their sensitivity to location accuracy.

To proceed, one considers the uniform grid $h\mathbb{Z}$ and a random variable X following the centered Gaussian law $\mathcal{N}(0, \lambda h)$ of standard deviation λh which gives the noised grid $X + h\mathbb{Z}$ whose perturbation amplitude is linked to the grid step h by means of the parameter λ.

When λ is small enough toward unity, one can expect the discrete PSE and finite differences are still comparable. Nevertheless, when λ increases, one will show below that discrete PSE is exhibits better quality than both standard PSE and standard finite difference scheme, until the noise is of order of size step.

This test is performed with the Gaussian scalar blob (27) of standard deviation $\sigma = 0.5$ introduced in section 3.3. One considers the discrete PSE scheme defined by formula (24) with the spherically symmetric stencil generator $\Theta(r) = (1 + r^p)^{-1}$ which gives more weight than previously to points outside the standard 7 point finite difference scheme.

Left pictures of figure 13 exhibits the relative $\mathbb{L}^2$ error on Laplacian of the blob described above on a grid 128^3 with respect to the noise amplitude λ, for finite differences, standard PSE and discrete PSE using the 1-, 2- and 3-neighborhood.

Two stencil generators for the PSE schemes are investigated on this figure 13, of the kind $\Theta(x) = (1 + |x|^p)^{-1}$ with $p = 8$ (top pictures), which gives a discrete PSE scheme with coefficients close to the standard finite difference scheme, and $p = 2$ (bottom pictures). Note that

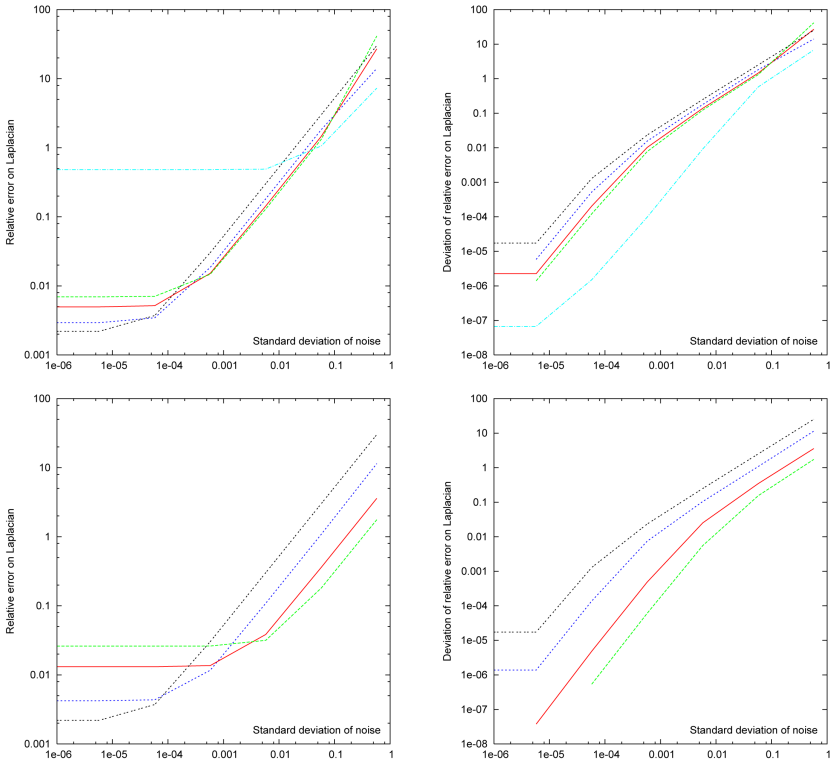

Figure 13: Relative errors on Laplacian of the Gaussian function (27) on a noised 3D lattice of size 128^3 (on left pictures) with respect to to noise standard deviation, and deviation of this error from the non-noised lattice (on right pictures). The curves concerns standard finite differences (dashed black), standard PSE (cyan), and discrete PSE with various stencil width ($h/\varepsilon = 1$ is dark blue, $h/\varepsilon = 2$ is red and $h/\varepsilon = 3$ is green). The PSE stencils are generated by two functions of the kind $\Theta(x) = (1 + |x|^p)^{-1}$ with $p = 8$ (top pictures) and $p = 2$ (bottom pictures).

the case $p = 2$ gives much more weight to particles in the neighborhood, due to the fact that Θ decreases much slower than for $p = 8$, but does not allow to define the classical formulation of particle strength exchange since the function $r^6/(1 + r^2)$ is not integrable over $\mathbb{R}_+$. Though the standard PSE is not plotted on bottom pictures of figure 13.

The right pictures of figure 13 exhibits the differences between errors with and without noise, *i*.e. the deviation from the relative non-noised error, which extracts the effects of noise on accuracy, thus defines a good criteria of sensitivity of the scheme to noise.

One can read on this figure that the error obtained when using discrete PSE using the 1-neighborhood is always smaller than finite differences of a factor 3 but exhibits an evolution of same rate as the noise amplitude factor λ increases, especially on the case $p = 8$. One can note the standard PSE is the less sensitive to noise but gives errors orders of magnitude higher, and becomes comparable to other schemes when the lattice is highly noised (top left picture of figure 13).

Furthermore, to increase accuracy, one can play with the stencil width to increase ε/h and then reduce the error shown to be of order $\mathcal{O}[(h/\varepsilon)^2]$. Indeed, one can see that if one uses the 2-neighborhood (or more), then accuracy is better than both standard PSE and finite differences. Indeed, it appears that the strongly weighted PSE (case $p = 2$, bottom pictures of figure 13) used with the 2- or 3-neightborhood is more accurate the finite differences as soon as particle positions

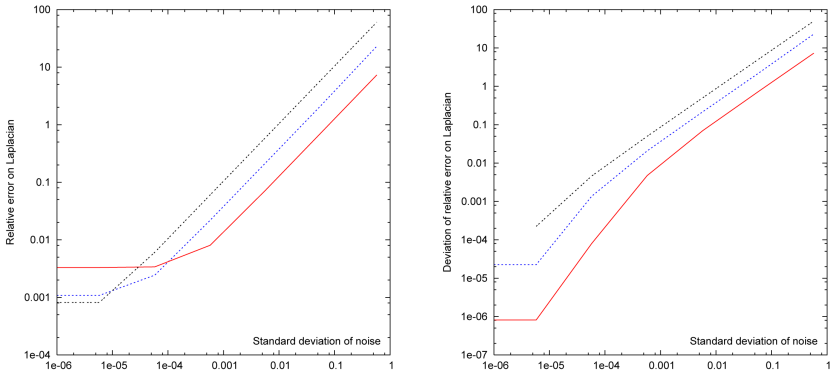

Figure 14: Same legend as figure 13 on a noised lattice of size 256^3 with the discrete PSE scheme generated by $\Theta(x) = (1 + |x|^2)^{-1}$.

are noised with a standard deviation $\sigma > 10^{-3}h$, (*i*.e. $\lambda > 10^{-3}$), and this with a lower sensitivity to noise.

To push further this conclusion, the case $p = 2$ has been reinvestigate on a finer grid of size 256^3, and the results displayed on figure 14. The conclusions for this more refined simulation are the same, and exhibits that accuracy of the discrete PSE scheme is 10 times better the finite differences as soon as the noise is sufficient ($\lambda > 10^{-4}$). Another formulation of this assertion is that the discrete PSE scheme provides the same accuracy for a noise ten times stronger.

8 Conclusion

In the present paper, one has defined a method of renormalization of particle strength exchange scheme whose resulting scheme can be assimilated to a finite difference stencil on uniformly discretized grid. One has shown that the same order of accuracy and convergence rate as standard 7 point finite difference scheme are reached, and this on various problems involving smooth and strongly discontinuous (random) fields of vorticity, scalar an vectorial problems, Cartesian and cylindrical coordinates, with and without boundary layers, and with various Reynolds numbers.

After exhibiting the same convergence rate than finite differences schemes, one has put the PSE schemes in their natural Lagrangian context and shown that discrete PSE is more accurate than finite differences. They appear to be faster and much easier to implement than adaptative (thus implicit) finite difference schemes. In other words, one gets an explicit one-pass scheme, to the opposite of renormalization process satisfying algebraic conservation of first moments (see [1]). One has also shown that standard PSE comes to be of the same order of accuracy for particle lattices strongly inhomogeneous.

As a conclusion one has built an easy to implement and accurate scheme which is effective both on uniformly discretized and Lagragian distribution. It can thus be used on both problems or with mixed Euler/Lagrangian formalism, used together or using Lagrangian scheme as a local refinement technique. The accuracy has been shown to be better than both finite differences and standard PSE for lattices moderately noised, which is the standard case in remeshed vortex in cell methods. This fact is especially interesting when viscous effects needs to be computed accurately, such as DNS of flows using particle methods at low and moderate Reynolds numbers.

References

[1] Brackbill J, Ruppel H 1986 A method for adaptively zoned, particle in cell calculations of fluids flows in two dimensions *J. Comp. Phys.* **65** 314–343.

[2] Cottet G-H, Koumoutsakos P D 2000 *Vortex methods, theory and practice* (Cambridge University Press).

[3] Cottet G-H, Koumoutsakos P D, Ould Sahili M L 2000 Vortex methods with spatially varying cores *J. Comp. Phys.* **162** 164–185.

[4] Cottet G-H, Poncet P 2002 Particle methods for Direct Numerical Simulations of three-dimensional wakes *J. Turbulence* **3**(038) 1–9.

[5] Cottet G-H, Poncet P 2003 Advances in Direct Numerical Simulations of three-dimensional wall-bounded flows by Particle in Cell methods *J. Comp. Phys.* **193** 136–158.

[6] Cottet G-H, Poncet P 2004 New results in the simulation and control of three-dimensional cylinder wakes *Comp. Fluids* **33** 687–713.

[7] Degond P, Mas-Gallic S 1989 The Weighted particle method for convection-diffusion equations *Math. Comput.* **53** 485–526.

[8] Hess J L 1990 Panel methods in computational fluid dynamics, *Ann. Rev. Fluid Mech.* **22** 255–274.

[9] Kim J, Moin P 1985 Application of a fractional-step method to incompressible Navier-Stokes equations *J. Comp. Phys.* **59** 308–323.

[10] Koumoutsakos P D, Leonard A, Pepin F 1994 Boundary conditions for viscous vortex methods *J. Comp. Phys.* **113** 52–61.

[11] Ould-Sahili M L , Cottet G-H, El Hamraoui M 2000 Blending finite-differences and vortex methods for incompressible flow computations *SIAM J. Sci. Comp.* **22** 1655–1674.

[12] Ploumhans P, Winckelmans G S, Salmon J K, Leonard A, Warren M S 2002 Vortex methods for direct numerical simulation of three-dimensional bluff body flows: application to the sphere at $\mathrm{Re} = 300, 500$, and 1000 *J. Comp. Phys.* **178** 427–463.

[13] Ploumhans P, Winckelmans G S 2000 Vortex methods for high-resolution simulations of viscous flow past bluff bodies of general geometry *J. Comp. Phys.* **165** 354–406.

[14] Poncet P 2002 Vanishing of mode B in the wake behind a rotationally oscillating circular cylinder *Phys. Fluids.* **14**(6) 2021–2023.

[15] Poncet P 2004 Topological aspects of three-dimensional wakes behind rotary oscillating cylinders *J. Fluid Mech.* **517** 27–53.